Microstructure-chemomechanics relations of polycrystalline cathodes in solid-state batteries

Avtar Singh [a,b], Jihun Song [e], Wei Li [e], Trevor Martin [d], Hongyi Xu [c], Donal P. Finegan [b], Juner Zhu [e,*]

[a] Department of Mechanical Engineering, Massachusetts Institute of Technology, 77 Mass Ave, Cambridge, MA 02139, United States of America
[b] Center for Energy Conversion and Storage Systems, National Renewable Energy Laboratory, Golden, CO 80401, United States of America
[c] Department of Mechanical Engineering, University of Connecticut, Storrs, United States of America
[d] Chemistry and Nanoscience Center, National Renewable Energy Laboratory, Golden, CO 80401, United States of America
[e] Department of Mechanical and Industrial Engineering, Northeastern University, 360 Huntington Ave, Boston, MA 02115, United States of America

ARTICLE INFO

ABSTRACT

Lithium-nickel-manganese-cobalt-oxides (NMC) embedded in solid-electrolytes are being extensively applied as composite cathodes to match the high energy density of metallic anodes. During charge/discharge, the cathode composite often degrades through the evolution of micro-cracks within the grains, along the grain boundaries, and delamination at the particle-electrolyte interface. Experimental evidence has shown that regulating the morphology of grains and their crystallographic orientations is an effective way to relieve the volume-expansion-induced stresses and cracks, consequently stabilizing the electrochemical performance of the electrode. However, the interplay among the crystal orientation, grain morphology, and chemo-mechanical behavior has not been holistically studied. In that context, a thermodynamically consistent computational framework is developed to understand the role of microstructural modulation on the chemo-mechanical interactions of a polycrystalline NMC secondary particle embedded in a sulfide-based solid electrolyte. A phase-field fracture variable is employed to consider the initiation and propagation of cracks. A set of diffused phase-field parameters is adopted to define the transition of chemo-mechanical properties between the grains, grain boundaries, electrolyte, and particle-electrolyte interfaces. This modeling framework is implemented in the open-source finite element package MOOSE to solve three state variables: concentration, displacement, and phase-field damage parameter. A systematic parametric study is performed to explore the effects of aspect ratio, the crystal orientation of grains, and the interfacial fracture energy through the chemo-mechanical analysis of the composite electrode. The findings of this study offer predictive insights for designing solid-state batteries that provide stable performance with reduced fracture evolution.

1. Introduction

All-solid-state batteries (ASSBs) with lithium metal anode have made tremendous advancement as a promising solution to the future of e-mobility due to their higher energy density and safety [1]. Sulfide-based solid electrolytes are among the most optimistic candidates because of their high ionic conductivity, cost competitiveness of their constituting elements, and possessing mechanical properties, allowing composite electrode preparation at room temperature [2]. These solid-electrolytes in combination with nickel-rich ($LiNi_xCo_yMn_{1-x-y}O_2$) cathode materials have achieved high initial capacities in many lab demonstrations [3–6]. Nevertheless, Ni-rich cathodes, when integrated with sulfide-based solid electrolytes, suffer rapid capacity fade, which

can be attributed to the electro-chemical–mechanical degradation of the composite cathode [7]. Following that, the mechanistic understanding of various degradation mechanisms is the key to stable performance and long lifespan of ASSBs.

Lithium-nickel-manganese-cobalt-oxides, typically known as NMC cathode, can deliver a high reversible capacity of above 200 mAh/g with a high working voltage range of 3 V 4.3 V (vs. Li^+/Li) [8]. Attempts have been made to improve the discharge capacity and to reduce the manufacturing cost of batteries by replacing expensive cobalt (Co) with nickel (Ni) [9,10]. Nonetheless, the increase in Ni content within these cathode materials causes capacity degradation and thermal runaway issues, which are required to be overcome before their

utilization in practical scenarios [11–13]. Recent experimental results showed that these limitations are largely influenced by the microstructural characteristics of cathode materials, i.e., aggregated spherical secondary particles composed of randomly oriented primary particles or grains [13–15]. On the one hand, the randomly oriented grains induce tortuous and prolonged lithium-ion transport pathways through the secondary particles due to grain boundaries and inconsistent crystallographic orientation [16,17]. On the other hand, the multiple phase transition during the insertion and extraction of chemical species originates from non-uniform expansion and contraction of lattice parameters, especially when the parameter x in $LiNi_xCo_yMn_zO_2$ is > 0.8 [13, 18]. Such an anisotropic volume change in Ni-rich oxide cathode materials could result in considerable micro-strains at the grain boundaries of randomly oriented primary particles [8]. Subsequently, micro-cracks nucleate and propagate within the cathode material, which are further responsible for the pulverization of secondary particles [19,20]. For solid-state batteries, the cracking of NMC particles and their debonding from solid electrolytes are more prominent than in liquid electrolytes due to volume change during charge/discharge cycles [21,22]. These fracture mechanisms are experimentally identified as one of the primary reasons for the rapid capacity degradation of NMC cathodes [23–25]. To enhance their energy density without compromising the cyclic stability, the chemical composition of NMC cathodes is modified using various doping elements (i.e., Al, Ti, B, Zr, Nb, W, and Mo) [26–29]. Numerous surface coating techniques are also performed to suppress the formation of a cathode electrolyte interphase (CEI) layer on the particle surface, prolonging cycle life [30,31]. Both coating and ion-doping of NMC cathodes showed a marginal effect on enhancing the cyclic stability desired for future energy storage applications [32]. Another technique, called microstructural modulation, has emerged as a promising tool to improve cyclic stability in the presence of highly anisotropic diffusion pathways and lattice expansion/contraction of NMC cathode materials. Various researchers have proposed using radially-aligned elongated grains in radial crystal orientations. They found that the capacity retention of radially-aligned grains is higher than the conventional cathode materials over prolonged charge/discharge cycles [8, 17,33–35]. Nevertheless, the underlying interplay between the microstructural modulation and fracture mechanisms remains unclarified. Therefore, the present work is dedicated to filling this gap with a specific case of a polycrystalline NMC particle embedded in a sulfide-based solid electrolyte.

Besides the aforementioned experimental efforts, several computational studies have been performed to evaluate the grain boundary fracture within polycrystalline cathode subjected to lithiation/delithiation [20,36–40]. These studies are restricted to the discrete inter-element-based cohesive zone model (CZM), which requires the crack path to be known a priori. A phase-field fracture model is a reliable tool to capture the arbitrary crack propagation within the heterogeneous cathode materials [41–43]. Many studies have successfully simulated crack nucleation and propagation within simplified electrode particles using phase-field fracture theory [44–47]. In a polycrystalline cathode, the factors responsible for the crack formation are material composition, shape and size of the primary and secondary particles, morphological and crystal orientation of grains, rate, and depth of charge/discharge, and a number of electrochemical cycles [13,24,48–54]. Although part of these factors has been studied numerically [55–58], a comprehensive understanding of combined multiple failure mechanisms, i.e., inter-granular, intra-granular, and particle–matrix interface fractures, has not been reported. In a recent study, Singh et al. 2022 [59] developed a thermodynamically consistent chemo-mechanical model to simulate the inter- and intra-granular fracture of the polycrystalline material matrix. They have simulated the nucleation and propagation of fracture for different grain sizes, matrix modulus, and charge rate conditions. By closely following the model developed by [59], the present work primarily focuses on alleviating the impact of chemo-mechanical

degradation by modifying the morphology and microstructure of active material particles. The main objective of the present article is to understand the role of microstructural modulation on the chemo-mechanical behavior of a polycrystalline cathode particle embedded in the solid electrolyte. In this regard, the simulations were performed with the anisotropic transport properties of lithium-ions in addition to the anisotropic expansion of grains. Furthermore, the rate-dependent phase-field fracture was implemented to accommodate the fast charging conditions. We also utilized the stress-spectral decomposition of strain energy to accurately avoid the evolution of phase-field fracture because of the generation of compressive stresses within anisotropic polycrystalline material. Finally, with the developed FE framework, we addressed the influence of crystallographic direction, the aspect ratio of grains, and interface fracture energy on the attendant fracture behavior for NMC-polycrystalline particles embedded in a sulfide-based solid electrolyte during the deintercalation process.

2. Inspirations from experimental observations

The research problem to be studied stems from our experimental observations [60]. Fig. 1(a) and (b) show the electron backscatter diffraction (EBSD) images of cross-sectioned NMC532 and NMC811 particles, respectively, alongside the r-orientation (i.e., the angle between radial direction and c-axis of NMC [15]) of the grains relative to the radial direction of the particle and the distribution of such. In the authors' recent publication [60], the NMC811 particle, a new generation of cathode materials, was shown to have more radially oriented grains than the NMC532 particle. The NMC532 and NMC811 particles underwent similar magnitudes of cracking (e.g. Fig. 1(c)), but the NMC811 particles were observed to maintain higher performance than the NMC532 particles. This was attributed to the more favorable orientation of the grains in the NMC811 particles. It should be noted that this is not a strict comparison because the chemical composition of the two materials is different. However, the material-level mechanical properties of NMC532 and NMC811 are close. We, therefore, can still attribute the stable performance of NMC811 to its microstructural modulation at the particle level. Furthermore, the previous work was conducted in a liquid electrolyte where cracks are expected to be infiltrated with the electrolyte and maintain or improve ion access to the particles. We acquired an X-ray nano-computed tomography (CT) image (Fig. 1(d)) of NMC particles in solid electrolyte and observed that certain regions of the interfacial contact between the particle and solid electrolyte can become detached following repeated cycling and morphological evolution of the NMC during operation. Additionally, unlike in liquid electrolyte cells, in solid electrolyte systems, the electrolyte will not infiltrate the cracks, which will exacerbate the effects of particle cracking. Therefore, we use this information to explore the cause and consequences of particle cracking in solid electrolyte systems and how to design particles with appropriate grain morphology that are preferable for reduced performance loss and long-life operation.

3. Chemo-mechanical model of heterogeneous electrode materials

A set of thermodynamic systems is utilized to explore the chemo-mechanical interactions by modulating the grains' morphology and crystallographic orientation for a polycrystalline cathode particle embedded in a solid-electrolyte. A schematic illustration of all-solid-state batteries consisting of two electrodes, a solid-electrolyte, and two current collectors is depicted in Fig. 2(a). We are particularly interested in the chemo-mechanical behavior of a polycrystalline cathode particle embedded in a solid-electrolyte as shown in Fig. 2(b). Accordingly, the present study only considers the solid electrolyte as a constraint to the deformation of the polycrystalline particle. For future studies, a thermodynamic consistent model will be developed for the solid-state battery, including the electric potentials, concentrations, mechanics, and fracture for the solid-electrolyte and electrode materials. A brief description of the kinematics and governing equations is provided below. For more detailed derivation, one can refer to an article by Singh and Pal, 2022 [59].
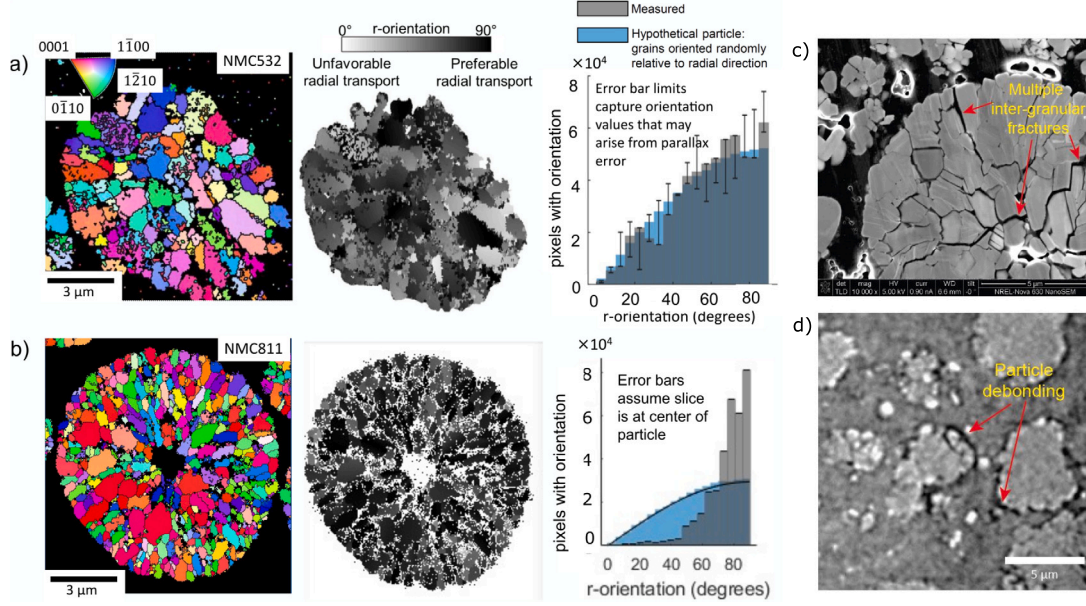
Fig. 1. EBSD inverse pole figure (IPF) maps of polycrystalline (a) NMC-532 and (b) NMC-811 with histograms illustrate the measure of crystal orientation of grains (reproduced from [60]) (c) SEM image showing several intergranular fractures within NMC811 particle (d) Slice view from X-ray computed tomography image depicting the delamination of argyrodite solid electrolyte from NMC811 particle.
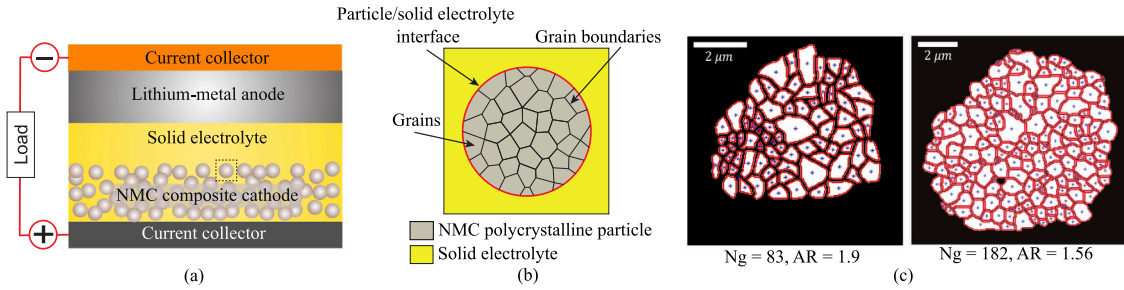

Fig. 2. (a) A Schematic representation of an all-solid-state battery system with multiple components, and (b) Zoomed view of a polycrystalline cathode particle embedded in a solid-state electrolyte. (c) Experimentally obtained images through Electron Back Scattering Diffraction (EBSD) technique for grain interior of different NMC particles [61,62].

3.1. Kinematics and field variables

Consider $\Omega \subset R^{n_{\dim}}$ ($n_{dim} = 1, 2, 3$) the arbitrary reference domain representing the chemo-mechanical system at time t with $n_{\dim}$ being the space dimension. The external boundary of domain Ω is defined as $\partial\Omega \subset R^{n_{\dim}-1}$ with $\boldsymbol{n}$ being the outward unit normal. Let $\boldsymbol{x}$ describe the spatial coordinates for the material points of solid within Ω. Subsequently, $c(\boldsymbol{x}, t)$ is the scalar field for the concentration of chemical species per unit volume, and $\boldsymbol{u}(\boldsymbol{x}, t)$ is the displacement vector defined as the kinematic descriptor for diffusion-induced deformation. To accommodate the initiation and propagation of the crack, a regularized scalar parameter $d(\boldsymbol{x}, t) : \Omega \subset R^{n_{\dim}}$ is adopted, which has a unit value on the fractured surface Γ_d and vanishes away from it. In general, the NMC-based cathode materials undergo smaller volume expansion/contraction of approximately 3.5% during insertion/extraction of lithium-ions [63]. Upon considering small strain deformation theory, the total strain tensor is additively decomposed into elastic $\boldsymbol{\varepsilon}_e$ and chemical part $\boldsymbol{\varepsilon}_c$, as follows.

$$\boldsymbol{\varepsilon} = \frac{1}{2}(\boldsymbol{u} + \boldsymbol{u}^T) = \boldsymbol{\varepsilon}_e + \boldsymbol{\varepsilon}_c,$$

$$\boldsymbol{\varepsilon}_c = (c - c_0)\boldsymbol{\beta}, \quad \boldsymbol{\beta} = \beta_{ij}\boldsymbol{e}_i \otimes \boldsymbol{e}_j, \tag{1}$$

in which c_0 is the initial or reference concentration within the host material, and $\boldsymbol{\beta}$ is the dilatational expansion tensor denoted as $\beta_{ij} = 0$ if $i \neq j$, and $\beta_{ij} \neq 0$ if $i = j$.

3.2. Total Helmholtz free energy

Within the chemo-mechanical-damage framework, the Helmholtz free energy density can be taken as a function of concentration, elastic strain, and phase field parameter such that $\Psi(c, \boldsymbol{\varepsilon}_e, d, \nabla d)$. Accordingly, the total energy contributions are divided into chemical part Ψ_c, elastic part Ψ_e and fracture part Ψ_f as

$$\Psi(c, \boldsymbol{\varepsilon}_e, d, \nabla d) = \Psi_c(c) + \Psi_e(\boldsymbol{\varepsilon}_e, c, d) + \Psi_f(d, \nabla d). \tag{2}$$

(A). $\Psi_c(c)$ is the non-uniform distribution of the concentration field with both entropic and energetic contributions as

$$\Psi_c(c) = RTc_{\max}[\tilde{c}\ln\tilde{c} + (1 - \tilde{c})\ln(1 - \tilde{c}) + \chi\tilde{c}(1 - \tilde{c})], \tag{3}$$

with chemical potential defined as the derivative of chemical free energy, such that

$$\mu = \frac{\partial\Psi_c}{\partial c} = RTc_{\max}\left[\chi(1 - 2\tilde{c}) + \ln\frac{\tilde{c}}{1 - \tilde{c}}\right] \tag{4}$$

in which χ is the Flory–Huggins binary interaction parameter which defines the miscibility gap between the two components or phases, R defines the gas constant, T denotes the reference temperature, $c_{\max}$ is the maximum solubility limit of the host lattice and $\tilde{c} = c/c_{\max}$ is the normalized concentration.
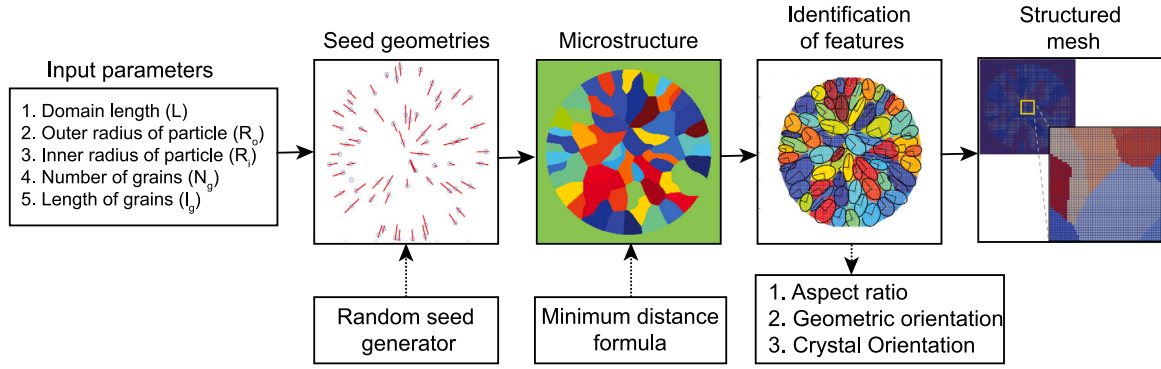
Fig. 3. Flow chart for the microstructure and mesh generation of a polycrystalline particle embedded in the matrix.

(B). Ψ_f is the dissipated fracture energy and is approximated as

$$\Psi_f(d, \nabla d) = \int_\Omega \mathcal{G}_c \left[\frac{1}{2l_d} d^2 + \frac{l_d}{2} \nabla^2 d \right] dV, \tag{5}$$

where $\mathcal{G}_c$ is the critical Griffith-type energy release rate for the fracture, and l_d is the regularization parameter that describes the actual thickness of the diffused crack. The phase field fracture approach resembles the traditional continuum damage models in which the scalar damage field may be rendered as the phase field parameter d. The loss of stiffness related to the mechanical degradation of the material is defined as a function of d. It is accomplished through monotonically decreasing energetic function $g(d) \in [0, 1]$ that relates the stored bulk energy per unit volume to the strain energy density of the unbroken solid while satisfying the following properties [43]

$$g'(d) < 0 \quad \text{and} \quad g(0) = 1, \quad g(1) = 0, \quad g'(1) = 0. \tag{6}$$

(C). Ψ_e is the strain energy density. To avoid the propagation of cracks during the compression loading, we have divided the elastic energy density into tensile Ψ_e^+ and compressive parts Ψ_e^-, such that

$$\Psi_e = \left[(1-d)^2 (1-k) + k \right] \frac{1}{2} \sigma^+ : \varepsilon_e + \frac{1}{2} \sigma^- : \varepsilon_e, \tag{7}$$

where a numerical constant $k > 0$ is chosen to be as small as possible to ensure positive definiteness after the material is fully broken. The projection tensors are defined to separate the compressive and tensile parts of the stresses such that.

$$\sigma^+ = \mathbf{P}^+ \sigma_0,$$
$$\sigma^- = \mathbf{P}^- \sigma_0, \tag{8}$$

where the projection tensors are defined as $\mathbf{P}^+ = \partial \sigma^+ / \partial \sigma_0$ and $\mathbf{P}^- = \mathbf{I} - \mathbf{P}^+$. A linear elastic material response is considered, such that the stress tensor of the unbroken material is

$$\sigma_0 = \mathbf{C}(\theta) : \varepsilon_e, \tag{9}$$

where $\mathbf{C}(\theta)$ is the orientation-dependent fourth-order elasticity tensor, with as much symmetry as desired. To take into account the crystallographic direction of individual grains within the polycrystalline cathode, the orientation-dependent elastic stiffness tensor can be represented as [64]

$$\mathbf{C}(\theta) = \mathbf{Q}(\theta) \mathbf{C}_g \mathbf{Q}(\theta)^T, \tag{10}$$

where $\mathbf{C}_g$ is the elastic tensor in the grain coordinate system, and $\mathbf{Q}$ is the transformation matrix in Voigt's notation.

3.3. Governing equations

In the absence of any chemical reaction, the governing equations for the chemical equilibrium, along with the initial and boundary conditions, are summarized as follows:

$$\begin{cases} \dfrac{\partial c}{\partial t} + \nabla \cdot \mathbf{J} = 0 & \forall \mathbf{x} \in \Omega, \\ c = c_p & \text{on } \Gamma_c, \\ \mathbf{J} \cdot \mathbf{n} = J_p & \text{on } \Gamma_J, \\ c(\mathbf{x}, 0) = c_0(\mathbf{x}) & \forall \mathbf{x} \in \Omega, \end{cases} \tag{11}$$

in which $\mathbf{J}$ is the diffusional flux through the cathode and can be defined as

$$\mathbf{J} = -\mathbf{M} \nabla \mu = -\mathbf{M} \left[RT \left(\frac{1}{\tilde{c}(1-\tilde{c})} - 2\chi \right) \nabla \tilde{c} \right]. \tag{12}$$

where $\mathbf{M}$ is the concentration, damage, and orientation-dependent anisotropic mobility tensor for the insertion of lithium species as

$$\mathbf{M}(c, d, \theta) = (1-d)^2 c (1-\tilde{c}) \frac{\mathbf{D}}{RT}, \tag{13}$$

in which $\mathbf{D}$ is the orientation-dependent diffusion tensor for individual grains of the polycrystalline cathode material described as

$$\mathbf{D} = \mathbf{Q}(\theta) \mathbf{D}_g \mathbf{Q}(\theta)^T, \tag{14}$$

with $\mathbf{D}_g$ defines the diffusivity tensor in the grain coordinates for the anisotropic transport of lithium ions.

Upon neglecting the inertial and body forces, the mechanical equilibrium equation, together with boundary conditions, is defined as

$$\begin{cases} \nabla \cdot \sigma = \mathbf{0} & \forall \mathbf{x} \in \Omega, \\ \mathbf{u} = \mathbf{u}_p & \text{on } \Gamma_u, \\ \sigma \cdot \mathbf{n} = t_p & \text{on } \Gamma_t. \end{cases} \tag{15}$$

Finally, the governing equation for the rate-dependent phase field fracture [43] is derived by taking the functional derivative of total free energy as $\dot{d} = -L \, \delta \Psi / \delta d$ and expressed along with the boundary conditions as follows.

$$\begin{cases} \dot{d} = -L \left[\mathcal{G}_c \left[\dfrac{d}{l_d} - l_d \nabla^2 d \right] - 2(1-d) \mathcal{H} \right] & \forall \mathbf{x} \in \Omega, \\ \nabla d \cdot \mathbf{n} = 0 & \text{on } \partial \Omega, \end{cases} \tag{16}$$

where L is the mobility parameter associated with the phase field fracture, and $\mathcal{H}$ is the history variable for avoiding crack healing during the evolution of phase-field fracture. More specifically, a history variable $\mathcal{H}$ is defined as the maximum energy density over the time interval $\tau = [0, t]$ with t denoting the current time step and expressed as

$$\mathcal{H} = \max_{\tau \in [0, t]} \left\{ \Psi_e^+ \right\}. \tag{17}$$

3.4. Diffused interface model

To handle the discontinuities in the material properties of interfaces and the bulk, a set of auxiliary field variables $\eta_1(\mathbf{x})$ and $\eta_2(\mathbf{x})$ for grain boundaries and particle/solid-electrolyte interface, respectively
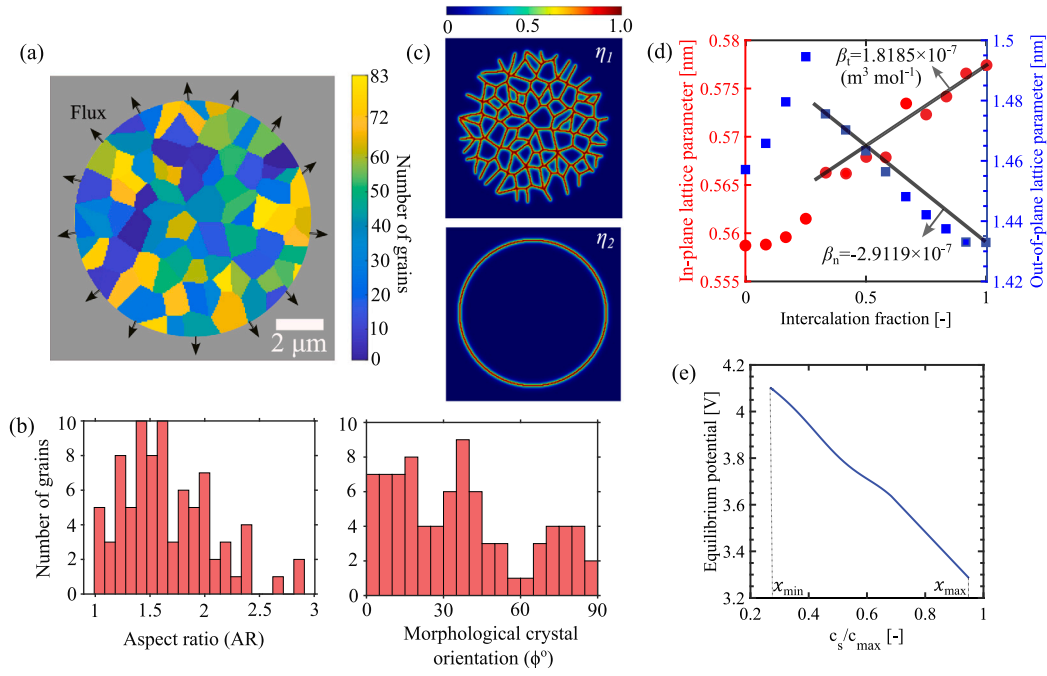
Fig. 4. (a) Polycrystalline particle embedded in solid-electrolyte subjected to constant flux boundary condition over the surface of the particle. All four corners of the domain are fixed, and periodic boundary conditions are enforced on all four sides of the domain. (b) Distribution of aspect ratio and morphological crystal orientation for individual grains. (c) Distribution of diffused interface parameters illustrating the grain boundaries η_1 and particle/solid-electrolyte interface η_2. (d) Anisotropic expansion coefficient for NMC811 upon lithium deintercalation [66]. The transverse and normal coefficients of expansion coefficients β_t and β_n are assumed as one-third of the ratio of normalized change in length over a change in concentration in the range of interest. (e) Equilibrium potential of the NMC cathode [67].

are introduced. The strong form of the interface phase field model, along with the boundary conditions, can be specified as

$$\begin{cases} \eta_k - l_k^2 \nabla^2 \eta_k = 0 & \text{in} \quad \Omega, \\ \eta_k(0) = 1 & \text{on} \quad \Gamma_k, \\ \nabla \eta_k \cdot \boldsymbol{n} = 0 & \text{in} \quad \partial\Omega. \end{cases} \tag{18}$$

in which the interface phase field $\eta_k(x)$ can be solved once the locations and material properties of the interface are determined. The extreme values $\eta_k = 1$ and $\eta_k = 0$ signify the interface and the bulk material. While $0 < \eta_k < 1$ describes the transition zone between the interface and bulk whose width is controlled by interface phase-field length scale l_k. To define the smooth variation of material properties within the transition zone of grains, grain boundaries, and particle/solid-electrolyte interface, an equivalent material property [65] is introduced as

$$\begin{aligned} \Theta^s(\eta_1, \eta_2) = & h_1(\eta_1) h_2(\eta_2) \Theta^G + [1 - h_1(\eta_1)] \Theta^{GB} \\ & + [1 - h_2(\eta_2)] \Theta^{PMI}, \end{aligned} \tag{19}$$

in which Θ^G, Θ^{GB}, and Θ^{PSI} are the material properties of grains, grain boundaries, and particle/solid-electrolyte interface, respectively. A quadratic function of $h_k = (1 - \eta_k)^2$ is considered to ensure that the equivalent properties at extreme values should degenerate to the original ones, and for the rest of the cases, the properties change continuously and monotonously [65].

To solve the coupled set of discretized equations, the finite-element-based open-source Multiphysics Object-Oriented Simulation Environment (MOOSE) simulation platform [68,69] is utilized.

4. Microstructure and mesh generation

To understand the role of microstructural modulation, microstructures with controlled features are generated by varying the aspect ratio, geometrical orientation, and crystallographic orientation of grains. These microstructures are generated by following steps mentioned in Fig. 3: (a) packing the seed geometries within the circular domain, (b) tessellating the seeds into polygonal grains using equidistant distance formula, (c) identification of microstructural features by fitting grains

within the ellipses, and (d) structured meshing to create a quadrilateral mesh.

5. Results and discussion

We investigated the role of microstructural modulation, i.e., the crystallographic direction and aspect ratio of grains subjected to galvanostatic charging (constant flux) conditions for spatial fracture evolution (Fig. 4(a)). The distribution of aspect ratio and morphological orientation of grains are provided in Fig. 4(b). Further, the diffused interface parameters representing the grain boundaries (η_1) and particle/solid-electrolyte interface (η_2) are illustrated in Fig. 4(c). To simulate the realistic condition of a NMC-polycrystalline particle, the geometric parameters such as the number and average aspect ratio of grains is extracted from the processed Electron Backscattering Diffraction (EBSD) images shown in Fig. 2(c). As per the parameters obtained and for simplicity, the total number of grains inside a particle and their average aspect ratio are assumed to be $N_g = 83$ and AR = 1.6, respectively. At the beginning, the intercalation state of the cathode particle is assumed to be $x = 0.95$ in $\text{Li}_x\text{NiMnCoO}_2$, and the deintercalation process ends when the average surface concentration of the particle becomes $x = 0.27$. Further, the anisotropic expansion/contraction of the cathode particle is considered by approximating the values provided by Lim et al. 2018 [66] as given in Fig. 4(d). The equilibrium overpotential against the normalized surface concentration is provided in Fig. 4(e). To better correlate with the magnitude of stresses developed in three-dimensional microstructures, we consider the 2D plain strain approximation condition without chemical expansion in the out-of-plane direction [70]. Various parameters required for the subsequent simulations are shown in Table 1.

5.1. Crystal orientation

To understand the role of crystal directions on the chemo-mechanical behavior, the crystallographic orientation of grains with normal distribution having mean equal to $\bar{\theta} = 0^0$ and standard deviation varies from

Table 1
Material parameters of NMC-polycrystalline cathode and sulfide-based solid electrolyte.

Parameters	Values
Diffusivity	$\mathbf{D}_g = \begin{bmatrix} 10^{-13} & 0 \\ 0 & 10^{-15} \end{bmatrix}$ m²/s [58]
Interaction parameter	$\chi = 1$
C-Rate	1C
Gas constant	R = 8.314 J/mol/K
Temperature	T = 300 K
Faraday's constant	F = 96 485 C/mol
Reaction coefficient	$k = 1.9 \times 10^{-9}$ m²·⁵ mol⁻⁰·⁵/s
Density	4870 g/cm³
Maximum concentration	c_{max} = 51 554 mol/m³
Elastic modulus of cathode	E_P = 140 GPa [71]
Poisson ratio of cathode	$\nu_P = 0.3$ [72]
Elastic modulus of $Li_2S - P_2S_5$ solid-electrolyte	E_{SE} = 19 GPa [73]
Poisson ratio of matrix	$\nu_{SE} = 0.34$
Fracture energy	$\mathcal{G}_c^G = 2.5$ J/m² [66]
	$\mathcal{G}_c^{GB} = \mathcal{G}_c^{PMI} = 1$ J/m² [38]
	$\mathcal{G}_c^{SE} = 2.78$ J/m² [74]
Length scale parameter	$l_d = 2.75 \times 10^{-7}$ m
	$l_1 = l_2 = 1 \times 10^{-7}$ m

$s_\theta = 5^0$ to 90^0 are generated as shown in Fig. 5(a). The contour plots of the phase field fracture parameter at the end of the deintercalation cycle for the different distribution of crystal directions are plotted in Fig. 5(b). A significant fracture regime emerged for the radial distribution of crystal orientation ($s_\theta = 5^0$). Due to the deintercalation of chemical species in the radial direction, more circumferential or hoop stresses are generated, which leads to the evolution of radial fracture. The NMC-polycrystalline particle having radial crystal orientation with $s_\theta = 30^0$ shows the combination of radial and circumferential cracks. This is because the deviation from radial crystal orientation enhances the tendency of both radial and circumferential stress generation. However, the density of radial fractures is higher than the circumferential cracks. With the further increase in s_θ from 30^0 to 90^0, the crack density and length decrease significantly.

Further, the evolution of maximum damage value within the domain and volumetric average of von Mises stress generation is determined and illustrated in Fig. 5(c) and (d), respectively. With the increase s_θ from 5^0 to 90^0, the rate of fracture decreases with the phase field parameter reaches $d = 1$ significantly earlier for $s_\theta = 5^0$ and quite afterward for $s_\theta = 90^0$. The extent of deintercalation is reduced with the increase in $s_\theta = 5^0$ to 90^0, and hence, the crack density is considerably lowered. It should be noted that we are not considering the stress-induced diffusion coupling; therefore, the extent of deintercalation or depth of discharge is only attributed to either fracture and/or crystal orientation. During the beginning of the simulation, the von Mises stress is higher for the radial crystal orientation; however, the earlier fracture evolution reduces the magnitude of stress. At the end of the deintercalation process, the stress magnitude is highest for $s_\theta = 5^0$ and minimum for $s_\theta = 60^0$. Moreover, the voltage evolution for polycrystalline particle with different crystal orientation distributions are shown in Fig. 5(e). With the increase in the standard deviation of crystal orientation from $s_\theta = 5^0$ to 90^0, the arrival of terminal voltage expedites. It is because the higher the crack density occurred at the earlier phase of deintercalation, the more it will hinder the deintercalation; hence, reaching the terminal voltage will take longer. This result is one of the advanced analyses estimated by our model and is contradictory to the electrochemical analysis of liquid electrolyte-based cells. As the liquid electrolyte penetrates the cracks of the particles, the electrochemical performance of the particles is improved with the increase of active surface area. This is also because the electrochemical properties of the electrolyte such as migration, and diffusivity can be 2–5 orders higher than those of the active material [75]. However, in this case, the solid-electrolyte does not penetrate the cracks of the particle, the crack becomes a factor preventing deintercalation.

To perform the statistical analysis, we have generated five microstructure samples having equivalent radial crystal orientation with mean $\bar\theta = 0^0$ and standard deviation $s_\theta = 60^0$. Contour plots for phase-field fracture for the different samples having a normal distribution of radial crystal orientation at the end of deintercalation are illustrated in Fig. 6(a). The evolution of phase-field fracture within the cathode particle is mainly in the circumferential direction for all the samples. However, a few radial cracks have also emerged within the particle. Fig. 6(b–d) illustrates the evolution of maximum phase field parameter value, a volumetric average of von Mises stress, and voltage within the domain. For all samples with a similar standard deviation of crystal orientation, the volumetric average of von Mises stress and voltage evolution within the domain is bounded within the narrow region.

5.2. Aspect ratio

One of the major parameters of microstructural modulation is the aspect ratio of grains. As mentioned earlier, the radially oriented single crystal primary particles provide a simple and efficient method to enhance the performance and applicability of Ni-rich layered oxide cathode materials [8]. Accordingly, we conducted a parametric analysis to investigate the influence of the grain's aspect ratio on the chemo-mechanical behavior of NMC-polycrystalline particle embedded in the solid-electrolyte subjected to 1C charge rate condition. Therefore, the microstructures with varying aspect ratios (AR) from AR = 2 to 14 are generated. Further, the morphological orientation of the grains is assumed to be in the radial direction. It is because the researchers have pointed out that the radial morphological grains are favorable to the transport of chemical species without inducing significant intergranular strains; thus, they are less prone to fracture. The simulations are performed for normal distribution of crystal orientation having mean $\bar\theta = 0°$ and standard deviation $s_\theta = 60°$. Fig. 7(a) illustrates the contour plots of phase-field fracture parameters for different aspect ratios of grains having radial crystal orientation at the end of the deintercalation cycle. It can be seen that the fractured regime decreases by changing the aspect ratio from AR = 2 to 14, with a maximum crack density observed for AR = 2. It should be noted that AR = 14 signifies the complete radial grains having minimum grain boundaries along the radial direction. A similar pattern of minimum or negligible fracture is also observed by Xu and co-authors [8]. They have explained that the radially elongated grains have lesser intergranular stresses, which helps to reduce or eliminate the occurrence of fracture within the NMC-polycrystalline cathode. Even though the crack density is minimum for AR = 14, some circumferential cracks and partial damage zones within the grains or grain boundaries exist. The radial crystal orientation generates critical tensile radial stresses, resulting in circumferential cracks. However, the partial damage zone within the grains or grain boundaries exists as no sufficient driving force is available for further crack growth. There is always uncertainty for such needle-like grains if the radial cracks occur within the grains or grain boundaries, as the length scale parameter might have a higher value in comparison to the width of the grain. In this section, we formed polycrystal particle structures having radially oriented single crystal primary particles with different AR, and successfully simulated cracks occurring inside the particles. We believe that this modeling can directly interpret the experimental results of reduced cracks inside polycrystalline particles having radially oriented single crystal primary particles, which have not been exactly identified, so provides deep insight for particle design to reduce cracks.

Fig. 7(b) depicts the evolution of maximum phase field parameter value for polycrystalline particles having different aspect ratios of grains. For AR = 2, the plane field fracture parameter reaches the terminal value much earlier in comparison to AR = 4.85, 9, and 14, which attain terminal damage values at approximately the same time. Other than that, the rate at which the phase field parameter advances from 0 to 1 is decreased with the increase in the aspect ratio of grains. Fig. 7(c) illustrates the evolution of averaged von Mises stress within
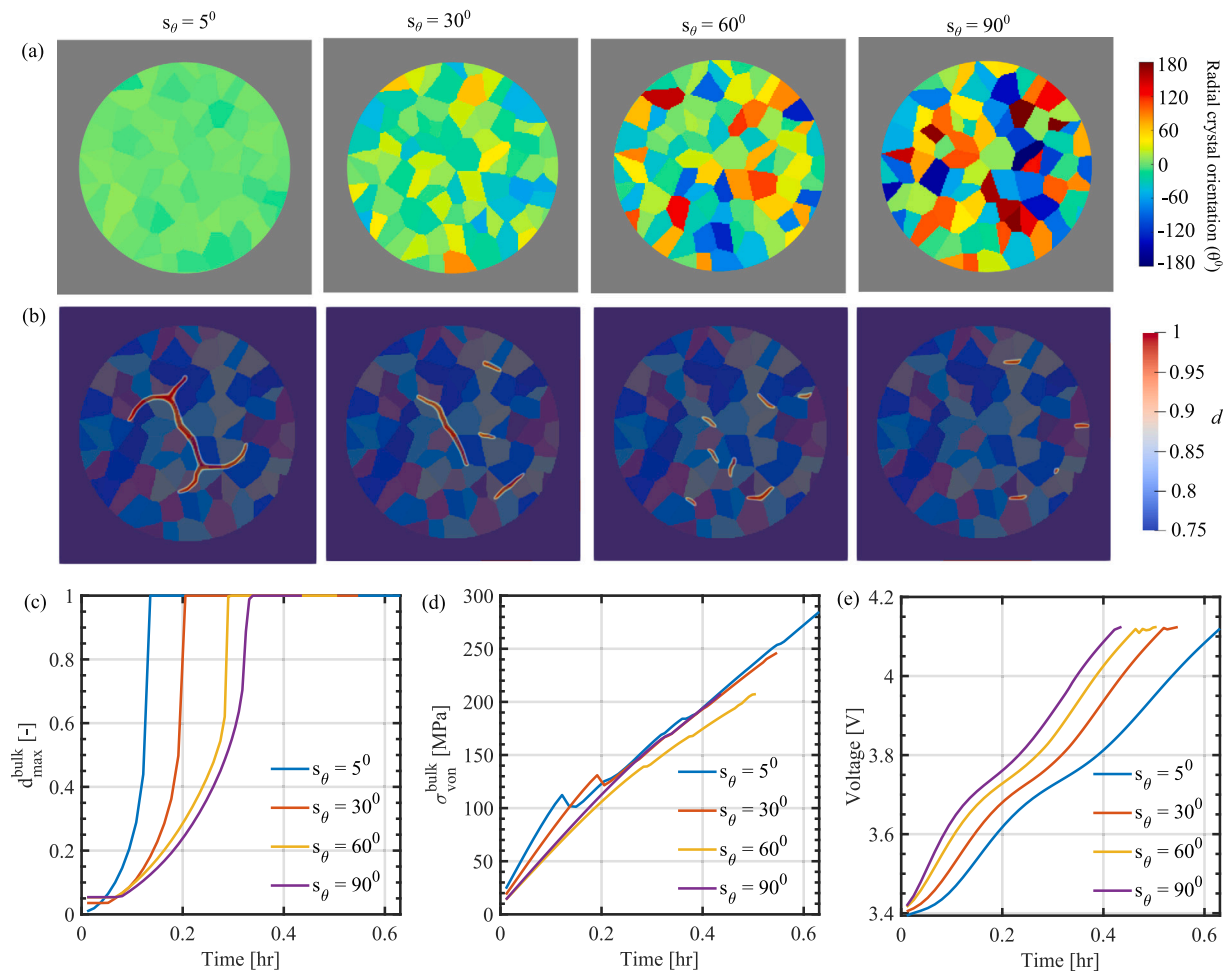
Fig. 5. (a) Contour plots illustrating the radial crystal orientation of grains having mean ($\bar{\theta} = 0^0$) and standard deviation varies from $s_\theta = 5^0$ to 90^0. (b) Contour plots of phase-field fracture parameters within the polycrystalline particle having various radial crystal orientations of grains. (c) Evolution for maximum phase field parameter value, and (d) the volumetric average of von Mises stress field within the domain. (e) Voltage vs time plot with voltage calculated using the average surface concentration of the particle. Simulations are performed for polycrystalline particle embedded in solid-electrolyte subjected to a deintercalation cycle at 1C C-rate condition.

the domain for various aspect ratios of grains. The average von Mises stress for all aspect ratios of grains lies within the narrow zone with a minimum value observed for AR = 4.85. Further, the voltage evolution for polycrystalline particles with grains having AR = 2 to 14 are plotted in Fig. 7(d). It shows that the higher the crack density, the higher the hindrance to the deintercalation; hence, reaching the terminal voltage will take longer. We have concluded that the aspect ratio of grains and crystal orientation predominantly alter the fracture behavior of NMC-polycrystalline particle embedded in solid-electrolyte.

5.3. Interface fracture energy

Besides the aspect ratio, tailoring the grain boundary properties is also found to be a classical protocol for reducing or preventing the disintegration of secondary particles. Recently, an experimental study has been performed to infuse the solid-electrolyte through the grain boundaries, which typically enhances the capacity retention and voltage stability of the NMC-cathode material [76] . Accordingly, the present section evaluates the effect of grain boundary fracture energy on the chemo-mechanical behavior of polycrystalline particle embedded in solid-electrolyte. For doing so, the polycrystalline particle having a grains aspect ratio of AR = 4.85 is considered, and the grain boundary fracture energy is varied from 0.5 to 4 J m^{-2}. We have assumed that fracture energies of the particle/solid-electrolyte interface remain constant for simplification.

Fig. 8(a) illustrates the pictograph of phase field parameter within the polycrystalline cathode particle having grain boundary fracture energy varies from $\mathcal{G}_c^{GB} = 0.5$ to 4 J m^{-2}. An increase in interface fracture energy from $\mathcal{G}_c^{GB} = 0.5$ to 4 J m^{-2} reduces the crack density; thus, the resistance to the crack propagation enhances, which hinders or eliminates the appearance of fracture. This is because the higher the interface fracture energy, the more will be the driving force required to initiate and propagate the crack within the domain. In particular, for $\mathcal{G}_c^{GB} = 0.5$ J m^{-2}, the maximum crack evolution can be seen in both radial and circumferential direction. However, for $\mathcal{G}_c^{GB} = 4$ J m^{-2}, no crack evolution occurred. Further, the maximum damage value within the domain is plotted over the deintercalation cycle in Fig. 8(b). It can be clearly seen that the rate at which the phase field fracture reaches its upper terminal value, i.e., d = 1 is highest for lower interface fracture toughness ($G_c = 0.5$ J m^{-2}) and decreases with the increase in interface fracture toughness from $\mathcal{G}_c^{GB} = 0.5$ to 2 J m^{-2}. For $\mathcal{G}_c^{GB} = 4$ J m^{-2}, the phase field parameter did not achieve its terminal value throughout the deintercalation cycle. Zhang et al. 2019 [77] have also observed a similar trend of a higher rate of increase in phase field fracture parameters for smaller fracture energy, which results in multiple cracks. Fig. 8(c) depicts the average von Mises stress within the domain. It can be observed that the magnitude of stresses within the polycrystalline cathode particle is enhanced with the increment in interface fracture energy. As mentioned previously, the higher the interface fracture energy, the more resistance to the driving force of fracture. Accordingly, the material will hold more stress before the crack initiation. Fig. 8(d)
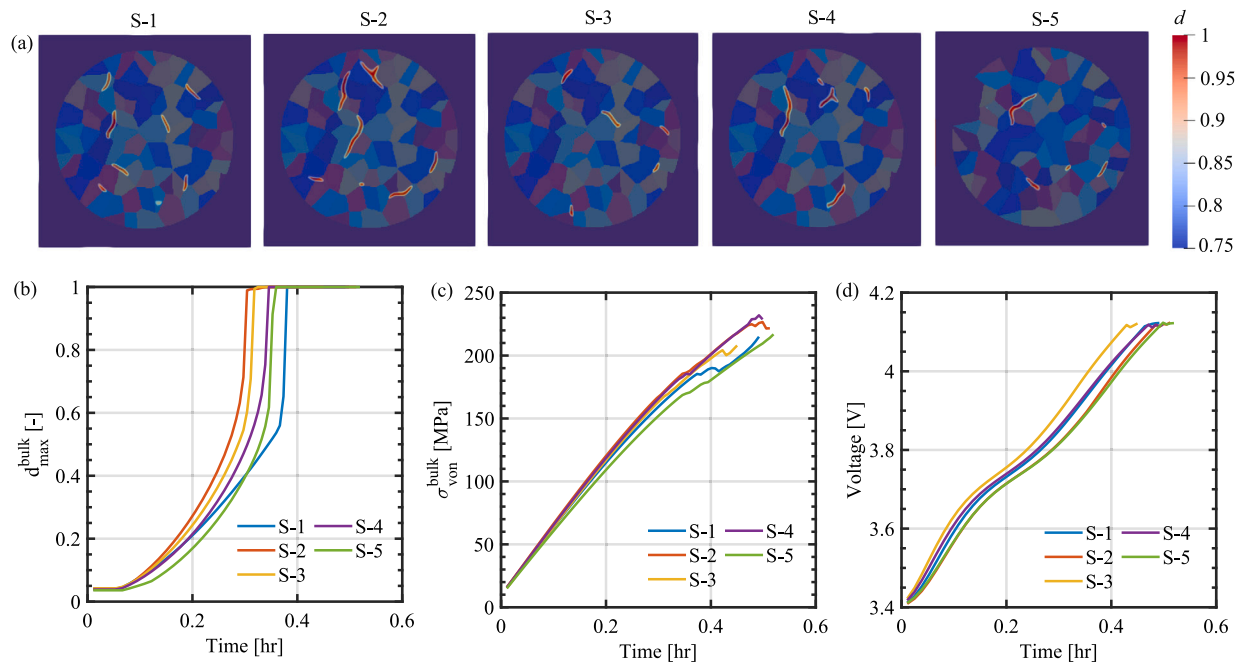
Fig. 6. (a) Contour plots of phase-field fracture parameters within the polycrystalline particle having radial crystal orientation of grains. (b) Evolution for maximum phase field parameter value, and (c) the volumetric average of von Mises stress field within the domain. (d) Voltage vs time plot with voltage calculated using the average surface concentration of the particle. For statistical analysis, all five samples have the same mean and standard deviation of radial crystal orientation, i.e., $\bar{\theta} = 0$ and $s_\theta = 60^0$. Simulations are performed for polycrystalline particle embedded in solid-electrolyte subjected to a deintercalation cycle at 1C C-rate condition.
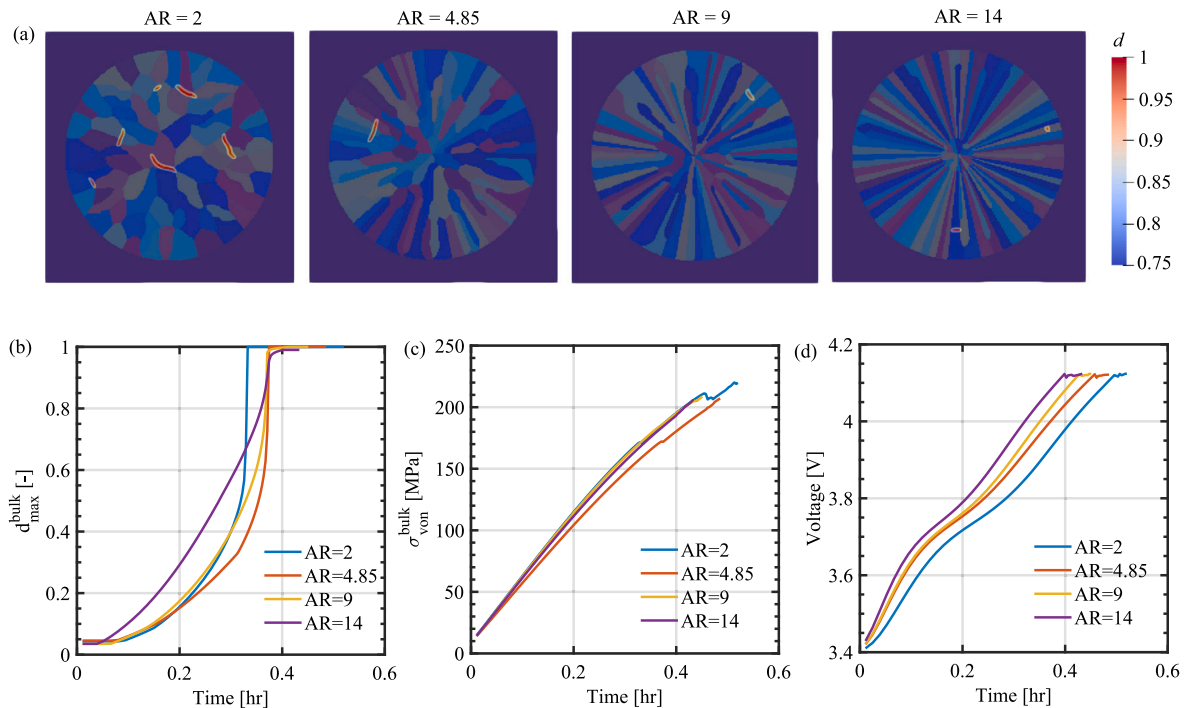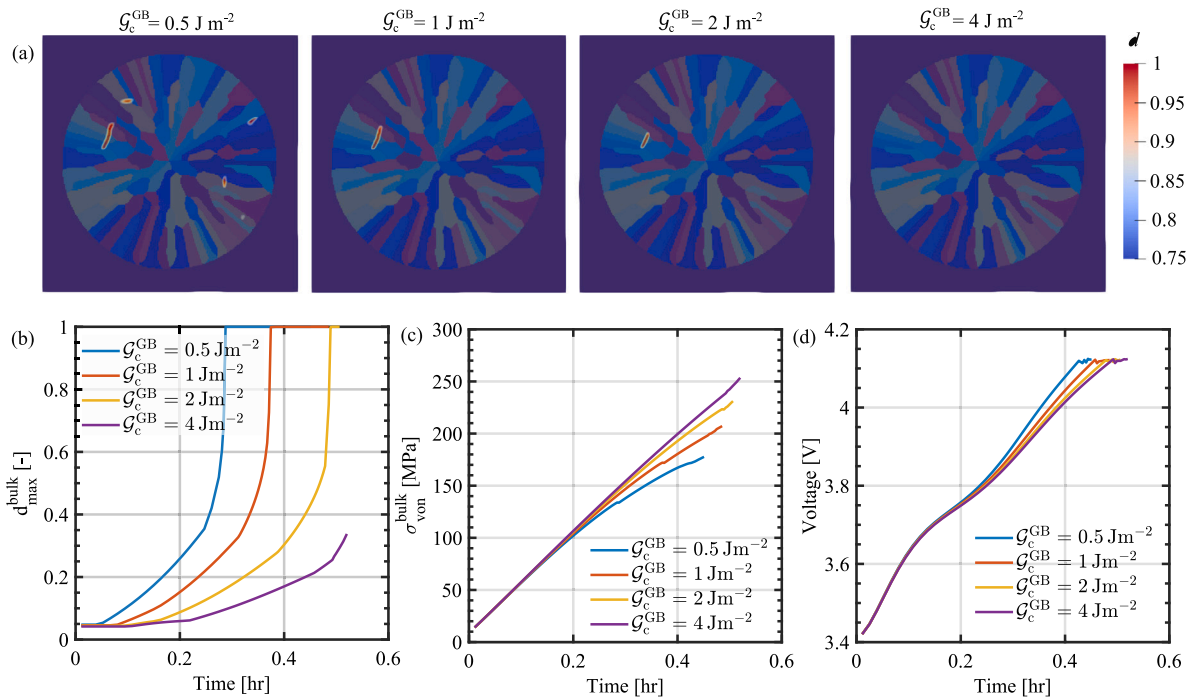

Fig. 7. (a) Contour plots of phase-field fracture parameters within polycrystalline particle having different aspect ratios of grains. (b) Evolution for maximum phase field parameter value, and (c) the volumetric average of von Mises stress field within the domain. (d) Voltage vs time plot with voltage calculated using the average surface concentration of the particle. Simulations are performed for polycrystalline particle with aspect ratios varying from 2 to 14 and subjected to deintercalation at 1C C-rate condition.

shows the voltage evolution with time, which illustrates that the lesser the interface energy, the faster it reaches the terminal voltage and vice-versa as per the rate of fracture evolution and diffusion hindrance caused by it. As mentioned earlier, the deintercalation can be affected by two factors: the crystal orientation and the evolution of fracture. In addition, the synergistic effect of crystal orientation and aspect ratio also plays a significant role in the deintercalation process. The present

section concludes that the change in interface fracture energy can significantly alter the chemo-mechanical behavior of NMC-polycrystalline particle embedded in sulfide-based solid-electrolytes.

In addition to the fracture toughness of grain boundaries, the particle–matrix interface can significantly alter the fracture behavior of polycrystalline particles embedded in solid electrolytes. Mechanical properties of the particle-SE interface can change with the type of solid

Fig. 8. (a) Contour plots of phase-field fracture parameters within polycrystalline particle having different aspect ratios of grains. (b) Evolution for maximum phase field parameter value, and (c) the volumetric average of von Mises stress field within the domain. (d) Voltage vs time plot with voltage calculated using the average surface concentration of the particle. Simulations are performed for polycrystalline particle with aspect ratios varying from 2 to 14 and subjected to deintercalation at 1C C-rate condition.

electrolyte, cathode, and their interactions, such as the CEI layer. Singh et al. (2022) [59] found that increasing the matrix's elastic modulus from 1 GPa to 100 GPa intensifies the crack density within the matrix. For matrix modulus greater than 30 GPa, significant particle–matrix interface debonding occurs. According to Park et al. 2023 [78] the CEI layer (formed by the oxidation of organic additives) has an elastic modulus that is similar to sulfide-based solid electrolytes ($E \leq 20$ GPa). Likewise, it should not significantly affect the crack propagation within the polycrystalline cathode particle. However, in general, the brittle and weak interface layer can restrict the volume change of cathode particles during charge/discharge, leading to particle-SE interface debonding and an increase in crack density within the polycrystalline cathode.

6. Conclusions

It is important to note that particle fracture will happen irrespective of the liquid- or solid-electrolyte. However, electrolyte infiltration will not occur in the case of solid-electrolyte, which further deteriorates the ionic path of chemical species. Therefore, the cathode particle design is more important for solid-electrolyte systems than liquid-electrolyte systems. In this regard, a chemo-mechanical model of an NMC polycrystalline particle was developed and comprehensively investigated the interplay among the crystal orientation, grain morphology, and chemo-mechanical behavior, which have been difficult to characterize experimentally and in previously developed models. Based on this comprehensive analysis, the brief succinct advice to cathode manufacturers for designing more robust polycrystalline particles for solid-electrolytes are: (1) Determining the critical crystal orientation for the synergistic effect of the better transport path, reduced stress generation, and lower crack density. This could already be realized by existing industrial techniques in the sintering process, as already witnessed in commercialized NMC811 products. (2) Generating elongated radial grains by increasing their aspect ratio for reduced crack density. This is also already

manageable with some reported technologies [8]. (3) Increasing the fracture toughness of interfaces to maintain the mechanical integrity of particles while electrochemical cycling which prevents the disruption of ionic pathways. One way is to infuse less stiff and high ductile solid-electrolyte into the grain boundaries [76].

Recent studies have investigated that solid-electrolytes show rate-dependent deformation behavior, which can significantly impact the overall performance of solid-state batteries [79,80], and will be incorporated into the present framework for future studies. Experimental quantification of stress along crack growth during chemo-mechanical loading is extremely challenging; however, the recent research shows promising results in probing stress along dendrite growth in solid electrolytes [81]. Another limitation of the proposed model is the inability to characterize chemo-mechanical behavior of grains smaller than the length scale parameter of phase-field fracture. For considering the small grains, one needs to refine the mesh so that the grain size should be considerably bigger than the length scale parameter, making the model computationally expensive. For such cases, simply reducing the length scale parameter and mesh size may result in under-predicting the fracture behavior. It is because, as mentioned in Appendix A.1, the maximum strength of the material will increase with a decrease in the length scale parameter (see Eq. (20)). As maximum strength is a material property, a grain size limit exists for simulating polycrystalline material with the proposed approach.

CRediT authorship contribution statement

Avtar Singh: Writing – original draft, Visualization, Validation, Software, Methodology, Investigation, Formal analysis. **Jihun Song:** Writing – review & editing, Validation, Software, Investigation. **Wei Li:** Software, Resources, Investigation, Conceptualization. **Trevor Martin:** Resources, Methodology, Data curation. **Hongyi Xu:** Validation, Supervision, Software, Methodology, Investigation, Formal analysis. **Donal P. Finegan:** Supervision, Methodology, Funding acquisition,

Formal analysis, Data curation, Conceptualization. **Juner Zhu:** Writing – review & editing, Supervision, Resources, Project administration, Methodology, Investigation, Funding acquisition, Data curation, Conceptualization.

Declaration of competing interest

Data availability

Data will be made available on request.

Acknowledgments

Appendix

A.1. Discussion on the choice of length scale parameters

The present model is comprised of three length scale parameters i.e., l_d, l_1, and l_2 which control the width of phase-field fracture zone, grain boundaries, and particle/solid-electrolyte interfaces, respectively. It should be mentioned that the length scale parameter in the phase field model plays a critical role in the initiation and propagation of fracture [82,83]. For example, the critical stress for the nucleation of the crack is inversely proportional to the square root of the length scale parameter. In that context, the length scale parameter can be determined in two ways, i.e., either assume length scale as a numerical parameter having value recommended to satisfy $l > 2h$ in which h defines the characteristic element length [43], or a material parameter whose value is a function of elastic modulus, fracture strength and fracture toughness of material [84] as follows

$$\sigma = \frac{9}{16}\sqrt{\frac{E\mathcal{G}_c}{3l_d}}. \tag{20}$$

In this study, the values of l_1 and l_2 are chosen to follow the $l_1, l_2 > 2h$ condition. Further, the length scale parameter l_d is adopted to follow even strict conditions of $l_d > 4h$ to accurately resolve the phase field fracture zone. We have performed the mesh convergence study (not reported here) to ensure that the fracture behavior is independent of the mesh size.

References

[1] J. Janek, W.G. Zeier, A solid future for battery development, Nat. Energy 1 (2016) 1–4.

[2] K.H. Park, Q. Bai, D.H. Kim, D.Y. Oh, Y. Zhu, Y. Mo, Y. Jung, Design strategies, practical considerations, and new solution processes of sulfide solid electrolytes for all-solid-state batteries, Adv. Energy Mater. 8 (2018) 1800035.

[3] Y.-G. Lee, S. Fujiki, C. Jung, N. Suzuki, N. Yashiro, R. Omoda, D.-S. Ko, T. Shiratsuchi, T. Sugimoto, S. Ryu, J.-H. Ku, T. Watanabe, Y. Park, Y. Aihara, D. Im, I.T. Han, High-energy long-cycling all-solid-state lithium metal batteries enabled by silver–carbon composite anodes, Nat. Energy 5 (2020) 299–308.

[4] S.H. Jung, U.-H. Kim, J.-H. Kim, S. Jun, C.S. Yoon, Y.S. Jung, Y.-K. Sun, Ni-rich layered cathode materials with electrochemo-mechanically compliant microstructures for all-solid-state Li batteries, Adv. Energy Mater. 10 (2020) 1903360.

[5] L. Zhou, C.Y. Kwok, A. Shyamsunder, Q. Zhang, X. Wu, L.F. Nazar, A new halospinel superionic conductor for high-voltage all solid state lithium batteries, Energy Environ. Sci. 13 (2020) 2056–2063.

[6] Y. Han, S.H. Jung, H. Kwak, S. Jun, H.H. Kwak, J.H. Lee, S.-T. Hong, Y.S. Jung, Single-or poly-crystalline Ni-rich layered cathode, sulfide or halide solid electrolyte: which will be the winners for all-solid-state batteries? Adv. Energy Mater. 11 (2021) 2100126.

[7] K.J. Kim, M. Balaish, M. Wadaguchi, L. Kong, J.L.M. Rupp, Solid-state Li-metal batteries: challenges and horizons of oxide and sulfide solid electrolytes and their interfaces, Adv. Energy Mater. 11 (2021) 2002689.

[8] X. Xu, H. Huo, J. Jian, L. Wang, H. Zhu, S. Xu, X. He, G. Yin, C. Du, X. Sun, Radially oriented single-crystal primary nanosheets enable ultrahigh rate and cycling properties of LiNi$_{0.8}$Co$_{0.1}$Mn$_{0.1}$O$_2$ cathode material for lithium-ion batteries, Adv. Energy Mater. 9 (2019) 1803963.

[9] P. Zhou, H. Meng, Z. Zhang, C. Chen, Y. Lu, J. Cao, F. Cheng, J. Chen, Stable layered Ni-rich LiNi$_{0.9}$Co$_{0.07}$Al$_{0.03}$O$_2$ microspheres assembled with nanoparticles as high-performance cathode materials for lithium-ion batteries, J. Mater. Chem. A 5 (2017) 2724–2731.

[10] X. Wang, Y.-L. Ding, Y.-P. Deng, Z. Chen, Ni-rich/Co-poor layered cathode for automotive Li-ion batteries: promises and challenges, Adv. Energy Mater. 10 (2020) 1903864.

[11] S.-M. Bak, E. Hu, Y. Zhou, X. Yu, S.D. Senanayake, S.-J. Cho, K.-B. Kim, K.Y. Chung, X.-Q. Yang, K.-W. Nam, Structural changes and thermal stability of charged LiNi$_x$Mn$_y$Co$_z$O$_2$ cathode materials studied by combined in situ time-resolved XRD and mass spectroscopy, ACS Appl. Mater. Interfaces 6 (2014) 22594–22601.

[12] S. Hwang, S.M. Kim, S.-M. Bak, S.Y. Kim, B.-W. Cho, K.Y. Chung, J.Y. Lee, E.A. Stach, W. Chang, Using real-time electron microscopy to explore the effects of transition-metal composition on the local thermal stability in charged Li$_x$Ni$_y$Mn$_z$Co$_{1-y-z}$O$_2$ cathode materials, Chem. Mater. 27 (2015) 3927–3935.

[13] H.-H. Ryu, K.-J. Park, C.S. Yoon, Y.-K. Sun, Capacity fading of Ni-rich Li [Ni$_x$Co$_y$Mn$_{1-x-y}$] O$_2$ ($0.6 \leq x \leq 0.95$) cathodes for high-energy-density lithium-ion batteries: Bulk or surface degradation? Chem. Mater. 30 (2018) 1155–1163.

[14] P. Yan, J. Zheng, M. Gu, J. Xiao, J.-G. Zhang, C.-M. Wang, Intragranular cracking as a critical barrier for high-voltage usage of layer-structured cathode for lithium-ion batteries, Nature Commun. 8 (2017) 1–9.

[15] A. Quinn, H. Moutinho, F. Usseglio-Viretta, A. Verma, K. Smith, M. Keyser, D.P. Finegan, Electron backscatter diffraction for investigating lithium-ion electrode particle architectures, Cell Rep. Phys. Sci. 1 (2020) 100137.

[16] G.-Z. Wei, X. Lu, F.-S. Ke, L. Huang, J.-T. Li, Z.-X. Wang, Z.-Y. Zhou, S.-G. Sun, Crystal habit-tuned nanoplate material of Li[Li$_{1/3-2x/3}$Ni$_x$Mn$_{2/3-x/3}$] O$_2$ for high-rate performance lithium-ion batteries, Adv. Mater. 22 (2010) 4364–4367.

[17] Y. Su, G. Chen, L. Chen, W. Li, Q. Zhang, Z. Yang, Y. Lu, L. Bao, J. Tan, R. Chen, S. Chen, F. Wu, Exposing the {010} planes by oriented self-assembly with nanosheets to improve the electrochemical performances of Ni-rich Li[Ni$_{0.8}$Co$_{0.1}$Mn$_{0.1}$] O$_2$ microspheres, ACS Appl. Mater. Interfaces 10 (2018) 6407–6414.

[18] J.-M. Lim, T. Hwang, D. Kim, M.-S. Park, K. Cho, M. Cho, Intrinsic origins of crack generation in Ni-rich LiNi$_{0.8}$Co$_{0.1}$Mn$_{0.1}$O$_2$ layered oxide cathode material, Sci. Rep. 7 (2017) 1–10.

[19] L. Mu, R. Lin, R. Xu, L. Han, S. Xia, D. Sokaras, J.D. Steiner, T.-C. Weng, D. Nordlund, M.M. Doeff, Y. Liu, K. Zhao, H.L. Xin, F. Lin, Oxygen release induced chemomechanical breakdown of layered cathode materials, Nano Lett. 18 (2018) 3241–3249.

[20] G. Sun, T. Sui, B. Song, H. Zheng, L. Lu, A.M. Korsunsky, On the fragmentation of active material secondary particles in lithium ion battery cathodes induced by charge cycling, Extreme Mech. Lett. 9 (2016) 449–458.

[21] R. Koerver, I. Aygun, T. Leichtweiss, C. Dietrich, W. Zhang, J.O. Binder, P. Hartmann, W.G. Zeier, J. Janek, Capacity fade in solid-state batteries: interphase formation and chemomechanical processes in nickel-rich layered oxide cathodes and lithium thiophosphate solid electrolytes, Chem. Mater. 29 (2017) 5574–5582.

[22] X. Liu, B. Zheng, J. Zhao, W. Zhao, Z. Liang, Y. Su, C. Xie, K. Zhou, Y. Xiang, J. Zhu, H. Wang, G. Zhong, Z. Gong, J. Huang, Y. Yang, Electrochemo-mechanical effects on structural integrity of Ni-rich cathodes with different microstructures in all solid-state batteries, Adv. Energy Mater. 11 (2021) 2003583.

[23] J.K. Rana, S. Glatthaar, H. Gesswein, N. Sharma, J.R. Binder, R. Chernikov, G. Schumacher, J. Banhart, Local structural changes in $LiMn_{1.5}Ni_{0.5}O_4$ spinel cathode material for lithium-ion batteries, J. Power Sources 255 (2014) 439–449.

[24] C.S. Yoon, D.-W. Jun, S.-T. Myung, Y.-K. Sun, Structural Stability of $LiNiO_2$ Cycled above 4.2 V, ACS Energy Lett. 5 (2017) 1150–1155.

[25] R. Li, W. Li, A. Singh, D. Ren, Z. Hou, M. Ouyang, Effect of external pressure and internal stress on battery performance and lifespan, Energy Storage Mater. 52 (2022) 395–429.

[26] S.-H. Han, J.H. Song, T. Yim, Y.-J. Kim, J.-S. Yu, S. Yoon, Communication—improvement of structural stability during high-voltage cycling in high-nickel cathode materials with B_2O_3 addition, J. Electrochem. Soc. 163 (2016) A748.

[27] D. Liu, S. Liu, C. Zhang, L. You, T. Huang, A. Yu, Revealing the effect of Ti doping on significantly enhancing cyclic performance at a high cutoff voltage for Ni-rich $LiNi_{0.8}Co_{0.15}Al_{0.05}O_2$ cathode, ACS Sustain. Chem. Eng. 7 (2019) 10661–10669.

[28] F. Xin, H. Zhou, X. Chen, M. Zuba, N. Chernova, G. Zhou, M.S. Whittingham, Li-Nb-o coating/substitution enhances the electrochemical performance of the $LiNi_{0.8}Mn_{0.1}Co_{0.1}O_2$ (NMC 811) cathode, ACS Appl. Mater. Interfaces 11 (2019) 34889–34894.

[29] T. Weigel, F. Schipper, E.M. Erickson, F.A. Susai, B. Markovsky, D. Aurbach, Structural and electrochemical aspects of $LiNi_{0.8}Co_{0.1}Mn_{0.1}O_2$ cathode materials doped by various cations, ACS Energy Lett. 4 (2019) 508–516.

[30] J. Cho, Y.J. Kim, B. Park, Novel $LiCoO_2$ cathode material with Al_2O_3 coating for a Li ion cell, Chem. Mater. 12 (2000) 3788–3791.

[31] S.-U. Woo, C.S. Yoon, K. Amine, I. Belharouak, Y.-K. Sun, Significant improvement of electrochemical performance of AlF_3-coated $Li[Ni_{0.8}Co_{0.1}Mn_{0.1}]O_2$ cathode materials, J. Electrochem. Soc. 154 (2007) A1005.

[32] U.-H. Kim, G.-T. Park, B.-K. Son, G.W. Nam, J. Liu, L.-Y. Kuo, P. Kaghazchi, C.S. Yoon, Y.-K. Sun, Heuristic solution for achieving long-term cycle stability for Ni-rich layered cathodes at full depth of discharge, Nat. Energy 5 (2020) 860–869.

[33] Z. Xu, Z. Jiang, C. Kuai, R. Xu, C. Qin, Y. Zhang, M. Rahman, C. Wei, D. Nordlund, C.-J. Sun, X. Xiao, X.-W. Du, K. Zhao, P. Yan, Y. Liu, F. Lin, Charge distribution guided by grain crystallographic orientations in polycrystalline battery materials, Nature Commun. 11 (2020) 1–9.

[34] G. Conforto, R. Ruess, D. Schröder, E. Trevisanello, R. Fantin, F.H. Richter, J. Janek, Quantification of the impact of chemo-mechanical degradation on the performance and cycling stability of NCM-based cathodes in solid-state Li-Ion batteries, J. Electrochem. Soc. 168 (2021) 070546.

[35] T.R. Tanim, P.J. Weddle, Z. Yang, A.M. Colclasure, H. Charalambous, D.P. Finegan, Y. Lu, M. Preefer, S. Kim, J.M. Allen, F.L.E. Usseglio-Viretta, P.R. Chinnam, I. Bloom, E.J. Dufek, K. Smith, G. Chen, K.M. Wiaderek, J.N. Weker, Y. Ren, Enabling extreme fast-charging: Challenges at the cathode and mitigation strategies, Adv. Energy Mater. 12 (2022) 2202795.

[36] R. Xu, K. Zhao, Corrosive fracture of electrodes in Li-ion batteries, J. Mech. Phys. Solids 121 (2018) 258–280.

[37] R. Xu, L.S. de Vasconcelos, J. Shi, J. Li, K. Zhao, Disintegration of Meatball Electrodes for $LiNi_xMn_yCo_zO_2$ Cathode Materials, J. Mech. Phys. Solids 58 (2018) 549–559.

[38] Y. Zhang, C. Zhao, Z. Guo, Simulation of crack behavior of secondary particles in Li-ion battery electrodes during lithiation/de-lithiation cycles, Int. J. Mech. Sci. (ISSN: 0020-7403) 155 (2019) 4802.

[39] R. Xu, K. Zhao, Electrochemomechanics of Electrodes in Li-Ion Batteries : A Review, J. Electrochem. Energy Convers. Storage 13 (2019) 1–9.

[40] A. Singh, S. Pal, Coupled chemo-mechanical modeling of fracture in polycrystalline cathode for lithium-ion battery, Int. J. Plast. 127 (2020) 102636.

[41] G.A. Francfort, J.-J. Marigo, Revisiting Brittle Fracture as an Energy Minimization Problem, J. Mech. Phys. Solids 35 (1998) 1319–1342.

[42] B. Bourdin, Numerical implementation of the variational formulation for quasi-static brittle fracture, Interfaces Free Bound. 9 (2007) 411–430.

[43] C. Miehe, F. Welschinger, M. Hofacker, Thermodynamically consistent phase-field models of fracture: Variational principles and multi-field FE implementations, Internat. J. Numer. Methods Engrg. 83 (2010) 1273–1311.

[44] L. Liang, M. Stan, M. Anitescu, Phase-field modeling of diffusion-induced crack propagations in electrochemical systems, Appl. Phys. Lett. 105 (2014) 163903.

[45] Y. Zhao, B.X. Xu, P. Stein, D. Gross, Phase-field study of electrochemical reactions at exterior and interior interfaces in Li-ion battery electrode particles, Comput. Methods Appl. Mech. Engrg. 312 (2016) 428–446.

[46] M. Klinsmann, D. Rosato, M. Kamlah, R.M. McMeeking, Modeling crack growth during Li insertion in storage particles using a fracture phase field approach, J. Mech. Phys. Solids 92 (2016) 313–344.

[47] B.-X. Xu, Y. Zhao, P. Stein, Phase field modeling of electrochemically induced fracture in Li-ion battery with large deformation and phase segregation, GAMM-Mitt. 39 (2016) 92–109.

[48] S. Zheng, R. Huang, Y. Makimura, Y. Ukyo, C.A. Fisher, T. Hirayama, Y. Ikuhara, Microstructural changes in $LiNi_{0.8}Co_{0.15}Al_{0.05}O_2$ positive electrode material during the first cycle, J. Electrochem. Soc. 158 (2011) A357–A362.

[49] G. Ćirić-Marjanović, Recent advances in polyaniline composites with metals, metalloids and nonmetals, Synth. Met. 170 (2013) 31–56.

[50] D.J. Miller, C. Proff, J.G. Wen, D.P. Abraham, J. Bareno, Observation of microstructural evolution in Li battery cathode oxide particles by in situ electron microscopy, Adv. Energy Mater. 3 (2013) 1098–1103.

[51] H.-H. Sun, A. Manthiram, Impact of microcrack generation and surface degradation on a nickel-rich layered Li $[Ni_{0.9}Co_{0.05}Mn_{0.05}]O_2$ cathode for lithium-ion batteries, Chem. Mater. 29 (2017) 8486–8493.

[52] L. Xia, D. Da, J. Yvonnet, Topology optimization for maximizing the fracture resistance of quasi-brittle composites, Comput. Methods Appl. Mech. Engrg. 332 (2018) 234–254.

[53] G. Li, Z. Zhang, Z. Huang, C. Yang, Z. Zuo, H. Zhou, Understanding the accumulated cycle capacity fade caused by the secondary particle fracture of $LiNi_{1-x}Co_xMn_yO_2$ cathode for lithium ion batteries, J. Solid State Electrochem. 21 (2017) 673–682.

[54] S. Xia, L. Mu, Z. Xu, J. Wang, C. Wei, L. Liu, P. Pianetta, Chemo-mechanical interplay of layered cathode materials undergoing fast charging in lithium batteries, Nano Energy 53 (2018) 753–762.

[55] W. Ai, B. Wu, E. Martínez-Pañeda, A coupled phase field formulation for modelling fatigue cracking in lithium-ion battery electrode particles, J. Power Sources 544 (2022) 231805.

[56] Y. Zhao, R. Wang, E. Martínez-Pañeda, A phase field electro-chemo-mechanical formulation for predicting void evolution at the Li-electrolyte interface in all-solid-state batteries, J. Mech. Phys. Solids (2022) 104999.

[57] A.M. Boyce, E. Martínez-Pañeda, A. Wade, Y.S. Zhang, J.J. Bailey, T.M. Heenan, D.J. Brett, P.R. Shearing, Cracking predictions of lithium-ion battery electrodes by X-ray computed tomography and modelling, J. Power Sources 526 (2022) 231119.

[58] J.M. Allen, P.J. Weddle, A. Verma, A. Mallarapu, F. Usseglio-Viretta, D.P. Finegan, A.M. Colclasure, W. Mai, V. Schmidt, O. Furat, D. Diercks, T.R. Tanim, K. Smith, Quantifying the influence of charge rate and cathode-particle architectures on degradation of Li-ion cells through 3D continuum-level damage models, J. Power Sources 512 (2021) 230415.

[59] A. Singh, S. Pal, Chemo-mechanical modeling of inter-and intra-granular fracture in heterogeneous cathode with polycrystalline particles for lithium-ion battery, J. Mech. Phys. Solids 163 (2022) 104839.

[60] T.R. Tanim, Z. Yang, D.P. Finegan, P.R. Chinnam, Y. Lin, P.J. Weddle, I. Bloom, A.M. Colclasure, E.J. Dufek, J. Wen, Y. Tsai, M.C. Evans, K. Smith, J.F. Allen, C.C. Dickerson, A.H. Quinn, A.R. Dunlop, S.E. Trask, A.N. Jansen, A comprehensive understanding of the aging effects of extreme fast charging on high Ni NMC cathode, Adv. Energy Mater. 12 (2022) 2103712.

[61] O. Furat, D.P. Finegan, D. Diercks, F. Usseglio-Viretta, K. Smith, V. Schmidt, Mapping the architecture of single lithium ion electrode particles in 3D, using electron backscatter diffraction and machine learning segmentation, J. Power Sources 483 (2021) 229148.

[62] O. Furat, L. Petrich, D.P. Finegan, D. Diercks, F. Usseglio-Viretta, K. Smith, V. Schmidt, Artificial generation of representative single Li-ion electrode particle architectures from microscopy data, Npj Comput. Mater. 7 (2021) 1–16.

[63] W.-S. Yoon, K.Y. Chung, J. McBreen, X.-Q. Yang, A comparative study on structural changes of $LiCo_{1/3}Ni_{1/3}Mn_{1/3}O_2$ and $LiNi_{0.8}Co_{0.15}Al_{0.05}O_2$ during first charge using in situ XRD, Electrochem. commun. 8 (2006) 1257–1262.

[64] T.T. Nguyen, J. Rethore, J. Yvonnet, M.-C. Baietto, Multi-phase-field modeling of anisotropic crack propagation for polycrystalline materials, Comput. Mech. 60 (2017) 289–314.

[65] P. Zhang, W. Yao, X. Hu, T.Q. Bui, 3D micromechanical progressive failure simulation for fiber-reinforced composites, Compos. Struct. 249 (2020) 112534.

[66] J.-M. Lim, H. Kim, K. Cho, M. Cho, Fundamental mechanisms of fracture and its suppression in Ni-rich layered cathodes: Mechanics-based multiscale approaches, Extreme Mech. Lett. 22 (2018) 98–105.

[67] K. Marker, P.J. Reeves, C. Xu, K.J. Griffith, C.P. Grey, Evolution of structure and lithium dynamics in $LiNi_{0.8}Mn_{0.1}Co_{0.1}O_2$ (NMC811) cathodes during electrochemical cycling, Chem. Mater. 31 (7) (2019) 2545–2554.

[68] D. Gaston, C. Newman, G. Hansen, D. Lebrun-Grandie, MOOSE: A parallel computational framework for coupled systems of nonlinear equations, Nucl. Eng. Des. 239 (2009) 1768–1778.

[69] C.J. Permann, D.R. Gaston, D. Andrš, R.W. Carlsen, F. Kong, A.D. Lindsay, J.M. Miller, J.W. Peterson, A.E. Slaughter, R.H. Stogner, R.C. Martineau, MOOSE: Enabling massively parallel multiphysics simulation, SoftwareX 11 (2020) 100430.

[70] K. Taghikhani, A. Singh, P. Weddle, A. Colclasure, K. Smith, J. Berger, R. Kee, Consequences of plane-strain and plane-stress assumptions in fully coupled chemo-mechanical li-ion battery models, Electrochimica Acta 479 (2024) 143790.

[71] R. Xu, H. Sun, L.S.D. Vasconcelos, K. Zhao, Mechanical and structural degradation of $Li_Ni_xMn_yCo_zO_2$ cathode in Li-ion batteries: an experimental study, J. Electrochem. Soc. 164 (2017) A3333.

[72] R. Xu, Y. Yang, F. Yin, P. Liu, P. Cloetens, Y. Liu, F. Lin, K. Zhao, Heterogeneous damage in Li-ion batteries: experimental analysis and theoretical modeling, J. Mech. Phys. Solids 129 (2019) 160–183.

[73] A. Sakuda, A. Hayashi, M. Tatsumisago, Sulfide solid electrolyte with favorable mechanical property for all-solid-state lithium battery, Sci. Rep. 3 (2013) 1–5.

[74] F.P. McGrogan, T. Swamy, S.R. Bishop, E. Eggleton, L. Porz, X. Chen, Y.-M. Chiang, K.J.V. Vliet, Compliant yet brittle mechanical behavior of Li_2S-P_2S_5 lithium-ion-conducting solid electrolyte, Adv. Energy Mater. 7 (2017) 1602011.

[75] J. Song, S.-H. Lim, K.-G. Kim, N. Umirov, H. Lee, C.B. Dzakpasu, J. Lim, J. Nam, J. Park, J.-N. Lee, H. Munakata, K. Kanamura, S.-S. Kim, Y.M. Lee, Digital-twin-driven diagnostics of crack propagation in a single $LiNi_{0.7}Mn_{0.15}Co_{0.15}O_2$ secondary particle during lithium intercalation, Adv. Energy Mater. 13 (2023) 202204328.

[76] P. Yan, J. Zheng, J. Liu, B. Wang, X. Cheng, Y. Zhang, X. Sun, C. Wang, J.-G. Zhang, Tailoring grain boundary structures and chemistry of Ni-rich layered cathodes for enhanced cycle stability of lithium-ion batteries, Nat. Energy 3 (2018) 600–605.

[77] Y. Zhang, C. Zhao, Z. Guo, Simulation of crack behavior of secondary particles in Li-ion battery electrodes during lithiation/de-lithiation cycles, Int. J. Mech. Sci. 155 (2019) 178–186.

[78] C. Park, J. Lee, S. Lee, Y.J. Han, J. Kim, S.-K. Jung, Organic-additive-derived cathode electrolyte interphase layer mitigating intertwined chemical and mechanical degradation for sulfide-based solid-state batteries, Adv. Energy Mater. 13 (16) (2023) 2203861.

[79] M. Papakyriakou, M. Lu, Y. Liu, Z. Liu, H. Chen, M.T. McDowell, S. Xia, Mechanical behavior of inorganic lithium-conducting solid electrolytes, J. Power Sources 516 (2021) 230672.

[80] C.E. Athanasiou, X. Liu, M.Y. Jin, E. Nimon, S. Visco, C. Lee, M. Park, J. Yun, N.P. Padture, H. H. Gao, B.W. Sheldon, Rate-dependent deformation of amorphous sulfide glass electrolytes for solid-state batteries, Cell Rep. Phys. Sci. 3 (2022) 100845.

[81] C.E. Athanasiou, C.D. Fincher, C. Gilgenbach, H. Gao, W.G. Carter, Y.-T. Chiang, B.W. Sheldon, Operando measurements of dendrite-induced stresses in ceramic electrolytes using photoelasticity, Matter 7 (1) (2024) 95–106.

[82] T.-T. Nguyen, J. Yvonnet, Q.-Z. Zhu, M. Bornert, C. Chateau, A phase-field method for computational modeling of interfacial damage interacting with crack propagation in realistic microstructures obtained by microtomography, Comput. Methods Appl. Mech. Engrg. 312 (2016) 567–595.

[83] A. Singh, T.S. Sandhu, S. Pal, Interplay of various fracture mechanisms in bio-inspired staggered structure, Mech. Mater. 139 (2019) 103215.

[84] H. Amor, J.-J. Marigo, C. Maurini, Regularized formulation of the variational brittle fracture with unilateral contact: Numerical experiments, J. Mech. Phys. Solids 57 (2009) 1209–1229.